SLAC-PUB-12545
astro-ph/0704.0255
June 2007

The Astrophysical Journal, submitted
Preprint typeset using LaTeX style emulateapj v. 10/09/06

# MODELING THE GALAXY THREE-POINT CORRELATION FUNCTION

Felipe A. Marín[1,*], Risa H. Wechsler[1,2], Joshua A. Frieman[1,3] and Robert C. Nichol[4]

*Submitted to The Astrophysical Journal*

## ABSTRACT

We present new theoretical predictions for the galaxy three-point correlation function (3PCF) using high-resolution dissipationless cosmological simulations of a flat ΛCDM Universe which resolve galaxy-size halos and subhalos. We create realistic mock galaxy catalogs by assigning luminosities and colors to dark matter halos and subhalos, and we measure the reduced 3PCF as a function of luminosity and color in both real and redshift space. As galaxy luminosity and color are varied, we find small differences in the amplitude and shape dependence of the reduced 3PCF, at a level qualitatively consistent with recent measurements from the SDSS and 2dFGRS. We confirm that discrepancies between previous 3PCF measurements can be explained in part by differences in binning choices. We explore the degree to which a simple local bias model can fit the simulated 3PCF. The agreement between the model predictions and galaxy 3PCF measurements lends further credence to the straightforward association of galaxies with CDM halos and subhalos.

*Subject headings:* cosmology: large-scale structure of universe — galaxies: formation — galaxies: statistics — galaxies: halos

## 1. INTRODUCTION

Observations of the higher-order statistics of the galaxy distribution can provide fundamental tests of the standard cosmological model. For example, higher-order correlation functions of the mass are predicted to be zero in linear perturbation theory for Gaussian initial conditions, which are expected in the simplest inflation models of the early Universe (Peebles 1980, Bernardeau et al. 2002, Szapudi 2005 and references therein). In the late Universe, however, non-linear gravitational clustering and biased galaxy formation lead to non-Gaussianity in the galaxy density field, resulting in non-zero connected N-point correlation functions (NPCFs) with $N > 2$. By studying higher-order galaxy statistics on large scales, we can test the nature of the initial conditions; on smaller scales, the NPCFs can constrain models of biased galaxy formation (e.g., Fry & Gaztanaga 1993; Frieman & Gaztanaga 1994) and the relationship between galaxies and their host dark matter halos.

The three-point correlation function (3PCF, or $\zeta$), and its Fourier-space equivalent, the bispectrum, are the first in the hierarchy of higher-order statistics and measure the shape dependence of the number of galaxy triplets as a function of scale. The 3PCF is sensitive to, for example, the shapes of dark matter halos and the presence of filamentary structures in the large-scale structure of the Universe (Sefusatti & Scoccimarro 2005). Since the pioneering work of Peebles and collaborators (see Peebles 1980 and references therein), there have been many measurements of the 3PCF and bispectrum using a variety of angular (Peebles & Groth 1975; Gaztanaga & Frieman 1994; Frieman & Gaztañaga 1999; Huterer et al. 2001; Szapudi et al. 2001, 2002; Ross et al. 2006) and redshift (Gaztanaga & Frieman 1994; Jing & Börner 1998; Verde et al. 1998; Scoccimarro et al. 2001; Feldman et al. 2001; Jing & Börner 2004) catalogs.

There has also been considerable theoretical work to understand the 3PCF and bispectrum using non-linear perturbation theory (see Bernardeau et al. 2002 and references therein) and cosmological simulations (Barriga & Gaztañaga 2002; Scoccimarro et al. 1999; Gaztañaga & Scoccimarro 2005; Hou et al. 2005).

In recent years, there has been renewed interest in the 3PCF due to the availability of large redshift surveys. These surveys now provide both the volume and the number of galaxies required to make robust measurements of the 3PCF over a range of scales. For example, recent papers by Kayo et al. (2004), Hikage et al. (2005), Nichol et al. (2006), Nishimichi et al. (2006), Kulkarni et al. (2007) have presented measurements of the 3PCF from the Sloan Digital Sky Survey (SDSS; York et al. 2000) as a function of scale, galaxy luminosity, and color. Nichol et al. (2006) also quantified the effect of large-scale structures on the shape dependence of the 3PCF. Likewise, several recent papers (Jing & Börner 2004; Baugh et al. 2004; Croton et al. 2004; Gaztañaga et al. 2005; Pan & Szapudi 2005; Croton et al. 2006) provide new measurements of the 3PCF and high-order correlations from the Two-degree Field Galaxy Redshift Survey (2dFGRS; Colless et al. 2001).

The main results from these recent SDSS and 2dFGRS analyses of the 3PCF are: *i)* on large scales, the observed 3PCF is in qualitative agreement with expectations for the growth of structure from Gaussian initial conditions; *ii)* on smaller scales (i.e., in the non-linear and weakly non-linear regimes), the 3PCF measured in redshift space scales with the redshift-space two-point correlation function (2PCF, or $\xi$) as $\zeta \sim \xi^2$, consistent with the "hierarchical clustering" ansatz (Peebles

[1] Department of Astronomy & Astrophysics, Kavli Institute for Cosmological Physics, The University of Chicago, Chicago, IL 60637 USA
[2] Kavli Institute for Particle Astrophysics & Cosmology, Physics Department, and Stanford Linear Accelerator Center, Stanford University, Stanford, CA 94305
[3] Center for Particle Astrophysics, Fermi National Accelerator Laboratory, P.O. Box 500, Batavia, IL 60510 USA
[4] Institute of Cosmology & Gravitation, University of Portsmouth, Portsmouth, PO1 2EG, UK
[*] e-mail: fmarinp@uchicago.edu

Work supported in part by US Department of Energy contract DE-AC02-76SF00515

1980); *iii)* the shape dependence of the reduced 3PCF depends at most weakly on galaxy luminosity; *iv)* the amplitude of the 3PCF is larger for elongated triangle configurations than for more symmetric triangle shapes (Gaztañaga & Scoccimarro 2005; Gaztañaga et al. 2005; Nichol et al. 2006; Kulkarni et al. 2007) — again consistent with expectations from non-linear clustering theory.

It is important to make detailed comparisons of these 3PCF observations with theoretical predictions that incorporate a realistic prescription for modeling galaxies and that account for observational effects such as redshift-space distortions. Such comparisons can be carried out in two ways: either the observations can be corrected for the redshift-space effects and compared to theory in real space, e.g., using the projected 3PCF (Zheng 2004), which is analogous to the projected 2PCF (Zehavi et al. 2005), or one can build mock galaxy catalogs from cosmological simulations and measure the theoretical 3PCF directly in redshift space. Since we also have access to the real-space 3PCF from such mock catalogs, we can investigate in detail the relationship between the real- and redshift-space correlation functions.

In this paper, we pursue the second of these methodologies, using state-of-the-art high-resolution dissipationless dark matter cosmological simulations. These simulations have the spatial resolution required to identify the dark matter (DM) halos and subhalos that host individual galaxies and at the same time encompass a large enough volume to probe large-scale structure in a statistically reliable way. The model we use assigns galaxy properties (luminosity, color, etc.) directly to these DM galactic halos and subhalos using simple, empirically-based assumptions about these properties. This approach differs in both assumptions and the resolution required from methods which build galaxy catalogs by statistically assigning several galaxies to each (more massive) halo using a Halo Occupation Distribution (HOD; e.g. Berlind & Weinberg 2002; see Kulkarni et al. (2007) for constraints on HOD parameters from the SDSS Luminous Red Galaxy sample's 3PCF) or from semi-analytic methods. The method used here was first implemented by Kravtsov et al. (2004), and has been applied successfully to different statistical studies, including the 2PCF (Conroy et al. 2006), galaxy-galaxy lensing (Tasitsiomi et al. 2004), and close pair statistics (Berrier et al. 2006) among others (see also Vale & Ostriker 2004, 2006; Conroy et al. 2007). Here we extend the study of this model to the 3PCF as a function of luminosity, color, and redshift. Where possible, we make direct comparisons in redshift space with recent observations.

In §2, we describe the simulations used in this paper and our methods for constructing mock galaxy catalogs based on resolved DM halos. We also review the techniques used to estimate the NPCFs. In §3, we present measurements of the 3PCF in both real and redshift space for both the dark matter and galaxy catalogs, while in §4, we study the dependence of the model 3PCF on galaxy luminosity and color. In §5, we compare the model 3PCF with SDSS observations and discuss the effects of binning. We relate the 3PCF to a simple non-linear bias model in §6. In §7, we summarize and discuss our findings.

## 2. METHODS

### 2.1. *Dark matter simulations*

We investigate clustering statistics using cosmological $N$-body simulations of structure formation in the concordance, flat ΛCDM cosmology with $\Omega_\Lambda = 0.7 = 1 - \Omega_m$, $h = 0.7$, and $\sigma_8 = 0.9$, where $\Omega_m$, $\Omega_\Lambda$ are the present matter and vacuum densities in units of the critical density, $h$ is the Hubble parameter in units of 100 km s$^{-1}$ Mpc$^{-1}$, and $\sigma_8$ specifies the present linear rms mass fluctuation in spheres of radius 8 $h^{-1}$Mpc. The simulations used here were run using the Adaptive Refinement Tree $N-$body code (ART, see Kravtsov et al. 1997 for details), which implements successive refinements in space and time in high-density environments. The primary simulation box we use is 120 $h^{-1}$Mpc on a side (hereafter, L120); the number and mass of each dark matter particle are $N_p = 512^3 \approx 1.34 \times 10^8$ and $m_p = 1.07 \times 10^9 h^{-1} M_\odot$ respectively. This simulation has been previously used to measure several properties of dark matter halos and subhalos (e.g., Allgood et al. 2006; Wechsler et al. 2006; Conroy et al. 2006; Berrier et al. 2006). In order to include more massive halos and study the effects of the size of the sample in the statistical analysis, we also use a second simulation with the same cosmological parameters in a bigger box, with 200 $h^{-1}$Mpc on a side (which was also used to measure halo shapes in Allgood et al. 2006). This box contains $N_p = 256^3$ particles with mass $m_p = 3.98 \times 10^{10} h^{-1} M_\odot$, therefore it will lack low mass (and luminosity) objects that are included in the L120 box.

From these dark matter samples, virialized concentrations of particles are identified as halos. In order to find these halos and their constituent subhalos (concentrations of virialized matter inside bigger halos), a variant of the Bound Density Maxima halo finding algorithm of Klypin et al. (1999) is used. This algorithm assigns densities to each particle using a smoothing kernel on the 32 nearest neighbors; centering on the highest-overdensity particle, each center is surrounded by a sphere of radius $r_{\rm find} = 50 h^{-1}$kpc. The algorithm removes unbound particles when calculating the properties of the halos.

Henceforth, we will use the terms "distinct halo" to mean any halo that is not within the virial radius of a larger halo, "subhalo" to indicate a halo that is within the virial radius of a larger halo, and "galactic halo" to refer to the halo directly hosting a galaxy. Using this terminology, the galactic halo of a satellite galaxy is a subhalo while the galactic halo of a central or isolated galaxy will be a distinct halo.

### 2.2. *From halos to 'galaxies'*

The primary galaxy samples used here are created by assigning galaxy luminosities and colors drawn from the SDSS redshift survey to dark matter halos and subhalos, using the maximum circular velocity at $z = 0$, $V_{\rm max}$, as an indicator of the halo virial mass. A luminosity (in the $r-$band) is assigned to each halo by matching the cumulative velocity function $n(> V_{\rm max})$ of all galactic halos (distinct halos and subhalos) to the observed SDSS $r$-band luminosity function (Blanton et al. 2003b) at $z = 0.1$ (the approximate mean redshift of the main spectroscopic SDSS galaxy sample used to estimate the luminosity function). To correct to $z = 0$ magnitudes,

TABLE 1
SUBSAMPLES AT $z = 0$

| Box | Subsample | Number of objects | Density $[(h^{-1}\mathrm{Mpc})^{-3}]$ |
|---|---|---|---|
| L120 | All objects $M_r^h < -19$ | 25371 | $1.5 \times 10^{-2}$ |
| L120 | $-19 < M_r^h < -20$ | 15432 | $8.9 \times 10^{-3}$ |
| L120 | $-20 < M_r^h < -21$ | 8153 | $4.7 \times 10^{-3}$ |
| L120 | red ($g - r > 0.7$) | 10059 | $5.8 \times 10^{-3}$ |
| L120 | blue ($g - r < 0.7$) | 15312 | $8.9 \times 10^{-3}$ |
| L200 | All objects $M_r^h < -20$ | 43564 | $5.4 \times 10^{-3}$ |
| L200 | $-20 < M_r^h < -21$ | 30575 | $3.8 \times 10^{-3}$ |
| L200 | $-21 < M_r^h < -22$ | 9921 | $1.2 \times 10^{-3}$ |
| L200 | red ($g - r > 0.7$) | 17278 | $2.2 \times 10^{-3}$ |
| L200 | blue ($g - r < 0.7$) | 23748 | $2.9 \times 10^{-3}$ |

we use the code `kcorrect v3_2` (Blanton et al. 2003a). Since the limited size of the box gives us an upper limit on the luminosities which can be reliably studied (in the statistical sense), and at the same time we cannot sample the lowest-luminosity objects due to limited spatial resolution, for the L120 box we present results for galaxies in the absolute magnitude range $-19 \geq M_r^h \geq -22$, where $M_r^h \equiv M_r - 5 \log h$. The L200 box has a lower resolution, therefore it contains only brighter objects, with $M_r^h \leq -20$. In order to assign colors to the galaxies, we use the procedure described by Wechsler (2004) and Tasitsiomi et al. (2004). This method uses the relation between local galaxy density (defined as the distance to the tenth nearest neighbor brighter than $M_r^h = -19.7$ and within $cz = 1000$ km/s) and color observed in the SDSS, using the CMU-Pitt Value Added Catalog constructed from DR1 (Abazajian et al. 2003), to assign a color to each mock galaxy. We use the distant observer approximation (Bernardeau et al. 2002) to obtain positions in redshift space. Table 1 describes the subsamples used in this study.

Although the general association of galaxies with dark matter subhalos seems quite robust, the detailed association of galaxy properties with subhalo properties is less clear. While galaxy luminosity is expected to be quite tightly connected to velocity, the circular velocity of a given subhalo decreases with time due to tidal stripping as it interacts with its host halo. Observable galaxy properties such as luminosity and color will likely be less affected by this process. This implies that galaxy observables may be more strongly correlated with $V_{\mathrm{max,acc}}$, the maximum circular velocity of the halos at the moment of accretion onto their host, than with the current maximum circular velocity, $V_{\mathrm{max,now}}$. This conclusion is supported by measurements of two-point statistics on both large and small scales in simulations (Conroy et al. 2006; Berrier et al. 2006). Motivated by these considerations, we construct galaxy catalogs using both $V_{\mathrm{max,acc}}$ and $V_{\mathrm{max,now}}$. We also use galaxy catalogs at different redshifts in order to study the evolution of the 3PCF with time. All these additional catalogs use the L120 box and have the same spatial density as the sample of halos selected by $V_{\mathrm{max,now}}$. We note that the model for assigning color is also not uniquely determined. It is, however, sufficient to match the two-point clustering length for red and blue galaxies and several observed properties of galaxy clusters (Zehavi et al. 2005). Future measurements of both clustering statistics and of the properties of galaxies in groups and clusters should help to further refine these galaxy assignment models.

### 2.3. *Measuring the 3PCF*

Just as the 2PCF measures the excess probability of finding two objects separated by a distance $r$, the 3PCF describes the probability of finding three objects in a particular triangle configuration compared to a random sample. The probability of finding three objects in three arbitrary volumes $dV_1$, $dV_2$ and $dV_3$ is given by (Peebles 1980)

$$P = [1 + \xi(r_{12}) + \xi(r_{23}) + \xi(r_{31}) + \zeta(r_{12}, r_{23}, r_{31})] \times \bar{n}^3 dV_1 dV_2 dV_3, \quad (1)$$

where $\bar{n}$ is the mean density of the objects, $\xi$ is the 2PCF, and $\zeta$ is the 3PCF:

$$\xi(r_{12}) = \langle \delta(r_1)\delta(r_2) \rangle \quad (2)$$

$$\zeta(r_{12}, r_{23}, r_{31}) = \langle \delta(r_1)\delta(r_2)\delta(r_3) \rangle; \quad (3)$$

here $\delta$ is the fractional overdensity in the dark matter field or in the distribution of galaxies. Since the 3PCF depends on the configuration of the three distances, it is sensitive to the 2-D shapes of the spatial structures, at large and small scales (Sefusatti & Scoccimarro 2005; Gaztañaga & Scoccimarro 2005). Motivated by the "hierarchical" form of the N-point functions, $\zeta \propto \xi^2$, found by Peebles & Groth (1975), we use the reduced 3PCF $Q(r, u, \alpha)$ to present our results:

$$Q(r, u, \alpha) = \frac{\zeta(r, u, \alpha)}{\xi(r_{12})\xi(r_{23}) + \xi(r_{23})\xi(r_{31}) + \xi(r_{31})\xi(r_{12})}. \quad (4)$$

This quantity is useful since $Q$ is found to be close to unity over a large range of scales even though $\xi$ and $\zeta$ vary by orders of magnitude (Peebles 1980). To parametrize the triangles for the 3PCF measurements, $r \equiv r_{12}$ sets the scale size of the triangle, while the shape parameters are given by the ratio of two sides of the triangle, $u = r_{23}/r_{12}$, and the angle between the two sides of the triangle $\alpha = \cos^{-1}(\hat{r}_{12} \cdot \hat{r}_{23})$, where $\hat{r}_{12}$, $\hat{r}_{23}$ are the unit vectors of the first two sides. Following Gaztañaga & Scoccimarro (2005), triangles where $\alpha$ is close to $0^\circ$ or $180^\circ$ are referred to as "elongated configurations", while those with $\alpha \sim 50^\circ - 120^\circ$ are referred to as "rectangular configurations",

We calculate the 2PCF using the estimator of Landy & Szalay (1993),

$$\xi = \frac{DD - 2DR + RR}{RR}. \quad (5)$$

Here, $DD$ is the number of data pairs normalized by $N_D \times N_D/2$, $DR$ is the number of pairs using data and random catalogs normalized by $N_D N_R$, and $RR$ is the number of random data pairs normalized by $N_R \times N_R/2$. The 3PCF is calculated using the Szapudi & Szalay (1998) estimator:

$$\zeta = \frac{DDD - 3DDR + 3DRR - RRR}{RRR}, \quad (6)$$

where $DDD$, the number of data triplets, is normalized by $N_D^3/6$, and $RRR$, the random data triplets, is normalized by $N_R^3/6$. $DDR$ is normalized by $N_D^2 N_R/2$, and $DRR$ by $N_D N_R^2$.

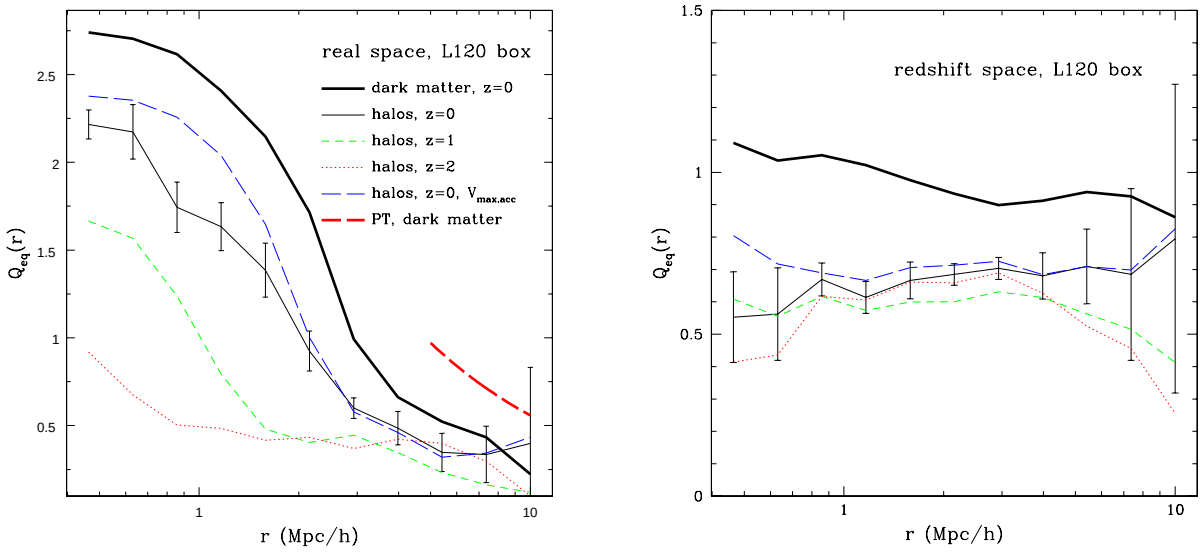


FIG. 1.— The reduced 3PCF, $Q_{eq}(r)$, for equilateral triangles in the L120 box. *Left:* Results in real space. *Thick solid line (black):* dark matter; *thin solid line (black):* galactic halos selected by $V_{max,now}$ at $z = 0$; *short-dashed (green):* galactic halos selected by $V_{max,now}$ at $z = 1$; *dotted (red):* galactic halos selected by $V_{max,now}$ at $z = 2$; *long-dashed (blue):* galactic halos selected by $V_{max,acc}$ at $z = 0$; *thick long-dashed (red):* leading-order perturbation theory, dark matter. *Right:* Results in redshift space. Line types correspond to the same dark matter and halo samples as in the left-hand plot. Error bars are calculated using jack-knife resampling and are only shown for one of the samples for clarity.

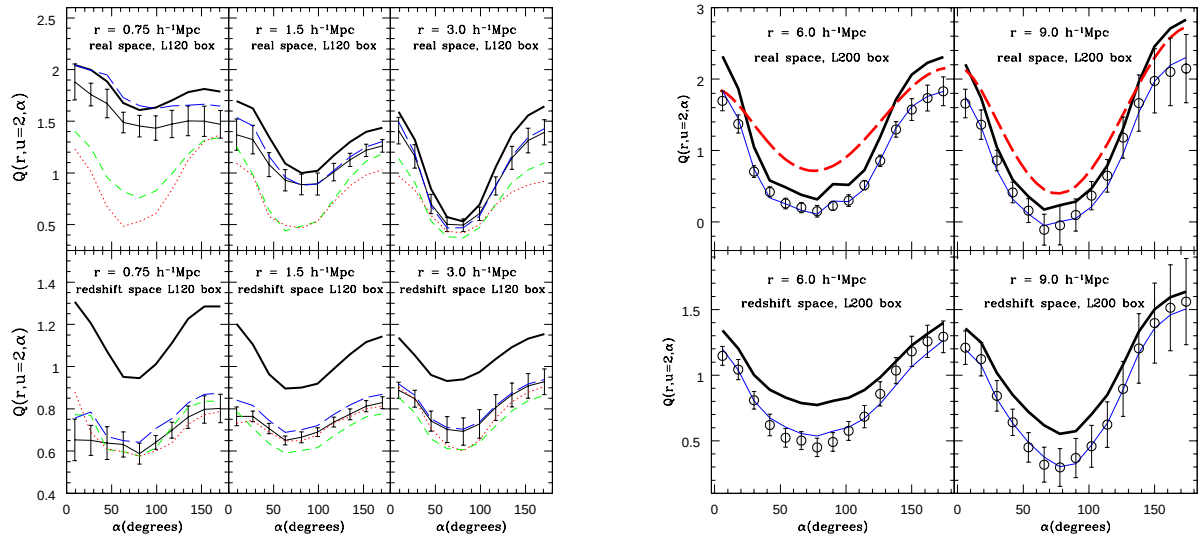


FIG. 2.— Measurement of the reduced 3PCF as a function of triangle shape, $Q(\alpha)$, for different scales $r$, with side ratio $u = r_{23}/r_{12} = 2$ fixed. *Left:* Results in the L120 box for $r = 0.75, 1.5$, and 3 $h^{-1}$Mpc (from left to right) in real space (top panels) and redshift space (bottom panels) for dark matter and galaxies; line types correspond to the same dark matter and halo samples as in Figure 1. *Right:* Results in the L200 box for $r = 6$ (left) and 9 $h^{-1}$Mpc (right) in real (top) and redshift space (bottom); *Thick solid line (black):* dark matter; *open circles:* galaxies in halos selected by $V_{max,now}$ at $z = 0$; *thin solid line (blue):* predicted galaxy 3PCF using the dark matter 3PCF $Q_{dm}$ and eqn. (10) with best-fit bias parameters $c_1, c_2$ obtained from fitting the galaxy 3PCF at $r = 9h^{-1}$ Mpc (see §6); *long dashed (red):* leading order non-linear perturbation theory prediction for dark matter reduced 3PCF. Error bars calculated using jack-knife resampling method.

We estimate the errors using jack-knife re-sampling. From each galaxy catalog, we construct sixteen subsamples of L120 or L200; within each of them we remove a different region $(30 \times 60^2$ $(h^{-1}\mathrm{Mpc})^3$ for the L120 box, and $50 \times 100^2$ $(h^{-1}\mathrm{Mpc})^3$ for the L200 box). The variance $\sigma_{JK}$ of $Q$ is calculated as:

$$\sigma^2_{JK} = \frac{N-1}{N} \sum_{i=1}^{N} (Q_i - \bar{Q}_i)^2, \qquad (7)$$

where $N = 16$ is the number of subsamples, $Q_i$ is the value for the $i-$th subsample, and $\bar{Q}_i$ is the mean of the $Q_i$. We note in passing that the validity of jack-knife resampling as a method to estimate the errors has not been explicitly tested with mock catalogs for three-point statistics. Although it is beyond the scope of this paper, this may be an interesting topic of future investigation especially once the statistical power of the measurements improves.

To compute the 2PCF and 3PCF, we use the *NPT* software developed in collaboration with the Auton Lab at Carnegie Mellon University. *NPT* is a fast implementation of the NPCFs using multi-resolution kd-trees to compute the number of pairs and triplets in a dataset. For more details and information on the algorithm, see Moore et al. (2001), Gray et al. (2004), and Nichol et al. (2006).

## 3. THE 3PCF OF GALAXIES AND DARK MATTER

We estimate the reduced 3PCF for the distribution of dark matter and for galaxies for different triangle configurations, focusing on the scale and shape dependence of the 3PCF. We also investigate its time evolution and how it depends on the selection criterion for subhalos. We study $Q(r, u, \alpha)$ in both real and redshift space, in order to compare our results with current observations and disentangle galaxy biasing effects from those which are consequences of redshift distortions.

In order to distinguish scale and, most importantly, shape effects, and to keep the errors as small as possible, we have chosen an intermediate-resolution binning scheme. For studies of equilateral triangles ($u = 1$ and $\alpha = \pi/3$ rad), we use bins of size $\Delta \log(r) = 0.1$. For measurements of the shape dependence of the 3PCF, we use triangles with four different scales $r_{12} = 0.75$, 1.5, 3, 6, and 9 $h^{-1}$Mpc, with scale bin size $\Delta r = 0.3r$ , shape parameter $u = 2$, and angular bin size $\Delta\alpha = \pi/15$ rad. This resolution is sufficient to see the most important features of the 3PCF even on small scales, although it is not sufficient to distinguish the "finger-of-god" effect at the smallest scales in redshift space, where $Q(\alpha)$ varies very little except at very small or elongated angles, where it increases to many times the mean value (Gaztañaga & Scoccimarro 2005).

### 3.1. *The 3PCF in real space*

Figures 1 and 2 show the 3PCF for dark matter particles and for galaxies from the L120 and L200 simulations. Here we plot results for dark matter (thick solid line), galaxies in halos selected by $V_{max,now}$ (thin solid line), and galaxies in halos selected by $V_{max,acc}$ (long-dashed line) for $z = 0$ and for halos selected by $V_{max,now}$ at $z = 1$ (short-dashed line) and $z = 2$ (dotted line).

Figure 1 shows the reduced 3PCF for equilateral triangles, $Q_{eq}(r)$, in real (left panel) and redshift space (right panel). In real space, the reduced 3PCF for the dark matter is only weakly scale dependent on small scales, decreases rapidly with increasing scale around $r \sim 3h^{-1}$ Mpc, and falls off more slowly on larger scales. This behavior is broadly consistent with previous N-body results (e.g. Scoccimarro et al. 1998) and with expectations from leading order non-linear perturbation theory on the largest scales (shown as the thick red long-dashed curve in Figure 1 left panel), with loop-corrected perturbation theory on intermediate scales where the rms perturbation amplitude $\delta(r)$ is of order unity (the transition to the strongly non-linear regime), and with quasi-stable hierarchical clustering on the smallest scales. Tests with the L200 box indicate that the downturn in $Q_{eq}$ for dark matter at scales larger than $r \sim 8h^{-1}$ Mpc is likely due to finite volume effects.

At scales below $r \sim 10h^{-1}$ Mpc, the dark matter $Q_{eq}$ is larger than that for the galaxies; this behavior is broadly expected if galaxies are more strongly clustered than (positively biased with respect to) the mass, cf. eqn.(10). At higher redshift, evolution is seen in $Q_{eq}(r)$ that is consistent with expectations from non-linear gravitational evolution: on the largest scales, the amplitude of $Q_{eq}$ is unchanging, as predicted from leading order perturbation theory, while the sharp break associated with the transition to the strongly non-linear regime moves to larger scales as the density perturbation amplitude increases with time.

Comparing results for subhalos selected by $V_{max,now}$ and by $V_{max,acc}$, differences in the amplitude of $Q_{eq}$ appear on small scales, $r \lesssim 3\ h^{-1}$ Mpc. In halo-model language, on these scales the 3PCF is sensitive to the internal structure of halos, i.e., to the one- and two-halo terms, while the three-halo term dominates the 3PCF on larger scales (Wang et al. 2004; Takada & Jain 2003).

In Figure 2, the top panels show how the reduced 3PCF depends on triangle shape in real space. In general, the 3PCF for elongated configurations is greater than for rectangular configurations. This is a consequence of the fact that, in non-linear gravitational instability, velocity flows tend to occur along gradients of the density field (Bernardeau et al. 2002). The 3PCF is larger for dark matter than for galaxies for all shapes and scales, although the difference is larger for elongated configurations. The difference in 3PCF amplitude between rectangular and elongated configurations is larger on large scales, in broad agreement with theoretical predictions (Bernardeau et al. 2002): on large scales, the strong shape dependence is determined by perturbative non-linear dynamics; on smaller scales, the shape dependence is washed out since the coherence between the velocity and density fields gives way to virialized motions. This scale dependence of the 3PCF shape is also reflected in the redshift evolution: in the L120 box (left panel), the galaxy 3PCFs at $z = 1$ and 2 (green-dashed and red-dotted curves) essentially retain the primordial shape dependence of leading-order non-linear perturbation theory, i.e., at those redshifts, these scales are still close to the quasi-linear regime. At $r = 3\ h^{-1}$Mpc, the largest evolution in $Q(\alpha)$ is found for elongated configurations.

As was seen in Figure 1, the effect of changing halo selection from $V_{max,acc}$ to $V_{max,now}$ on the 3PCF shape appears only on small scales, $r \lesssim 1.5h^{-1}$ Mpc, i.e., roughly within the scale of a typical cluster-mass host halo.

On the larger scales probed in the L200 box (right panel of Figure 2), the galaxy reduced 3PCF (open circles) tracks the shape of the dark matter 3PCF fairly well. The difference between the galaxy and dark matter 3PCF amplitudes on these scales is reasonably well fit by a simple bias prescription: the thin blue curve is the biased 3PCF that results from fitting the galaxy 3PCF with eqn. (10); see §6. We also see that the jack-knife errors increase on the largest scales, where the effects of the finite box size start to become evident. For comparison, the red long-dashed curve is the 3PCF of the dark matter from leading-order non-linear perturbation theory (Bernardeau et al. 2002; Jing & Borner 1997). On the largest scales, it is in reasonable agreement with the measured 3PCF for the dark matter.

### 3.2. *The 3PCF in redshift space*

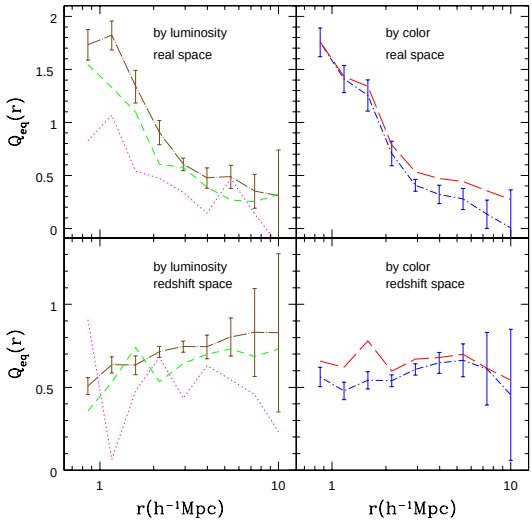


FIG. 3.— The reduced 3PCF, $Q(r)$, for equilateral triangles as a function of galaxy luminosity and color in real and redshift space. *Top left*: $Q_{eq}(r)$ in real space for galaxies divided into luminosity bins; *long dash-dotted (cyan):* $-19 > M_r^h > -20$; *short-dashed (green):* $-20 > M_r^h > -21$; *dotted (magenta):* $-21 > M_r^h > -22$. The brightest sample comes from the L200 box, the other two are from the L120 box. *Bottom left:* Results in redshift space; line types correspond to the same galaxy samples as in the top left panel. *Top right:* $Q_{eq}(r)$ in real space for galaxies divided according to color, using the L120 box; *long-dashed (red):* red galaxies ($g-r > 0.7$); *short dash-dotted (blue):* blue galaxies ($g-r < 0.7$). *Bottom right* Results in redshift space; line types correspond to the same galaxy samples as in the top right panel. Error bars are calculated using jack-knife respampling.

Redshift distortions have been studied in depth (and are a useful tool to constrain cosmological parameters) for the power spectrum (e.g., Bernardeau et al. 2002; da Ângela et al. 2005; Tinker 2007) and for the bispectrum (Scoccimarro et al. 1999; Verde et al. 2002; Sefusatti et al. 2006). Some comparisons have been made for the 3PCF as well (Matsubara & Suto 1994; Takada & Jain 2003; Wang et al. 2004). Gaztañaga & Scoccimarro (2005) found that the redshift distortions do not have a strong dependence on the cosmological parameters.

The right panel of Figure 1 and the bottom panels of Figure 2 show the 3PCF in redshift space. The first feature that can be seen is a dramatic decrease in the amplitude and in the scale and shape dependence of $Q$ compared to the real-space measurements. For example, for equilateral triangles, the redshift space $Q_z(r)$ is reduced compared to the real space $Q(r)$ at small scales and increased with respect to the real-space results on larger scales. The overall effect is that $Q_z(r)$ is nearly scale-independent, i.e., the clustering appears more hierarchical in redshift space (Suto & Matsubara 1994; Matsubara & Suto 1994; Scoccimarro et al. 1999). Moreover, in redshift space, the suppression of the galaxy 3PCF relative to that of the dark matter is apparent on all scales; it appears to be relatively independent of scale and configuration and is larger than the relative suppression in real space, consistent with earlier results (Wang et al. 2004; Gaztañaga et al. 2005). It also appears that there is very little redshift evolution of the galaxy 3PCF in redshift space; the measurements at $z = 1$ and $z = 2$ are nearly indistinguishable from each other. With regard to halo selection, as in real space we find that $Q_{Vmax,now} < Q_{Vmax,acc}$, but the differences between them are smaller than in real space.

Together, these results suggest that the shape and scale dependence of the reduced 3PCF in redshift space on the scales shown here are largely determined by redshift distortions, with non-linear gravitational evolution playing a subdominant role.

## 4. OBSERVING THE 3PCF: LUMINOSITY AND COLOR DEPENDENCE

To investigate the dependence of the three-point clustering on galaxy luminosity and color and to make direct comparisons with measurements from recent redshift surveys, we calculate the 3PCF for galaxies with luminosity and color cuts similar to those that have been applied to redshift survey data samples, with luminosity and color information obtained as described in §2. The luminosities are assigned according to $V_{max,now}$ in the L120 and L200 boxes. We adopt the same binning scheme used in the previous section.

### 4.1. *Luminosity dependence*

The left panels of Figure 3 show results for the reduced 3PCF for equilateral configuratons in two luminosity bins, in real and redshift space. For equilateral triangles, there is a small difference in 3PCF between the luminosity samples in real space: the fainter galaxies have larger $Q(r)$ than the brighter ones, as expected in a simple linear bias model (eqn. 10). The redshift-space 3PCFs for these galaxies are roughly constant with $r$, $Q_{z,gal}(r) \sim 0.7$, in agreement with SDSS measurements for these configurations (see Figures 7-9 in Kayo et al. 2004). There is a very slight difference between the reduced 3PCF amplitudes for different luminosity bins in redshift space, but it is not statistically significant for a dataset of this size. This result qualitatively agrees with the SDSS results of Kayo et al. (2004) who also found almost no luminosity dependence of the reduced 3PCF on these scales. They found a slightly higher amplitude for the reduced 3PCF for the $-19 > M_r^h > -20$ sample compared to that of brighter galaxies, but their results for the two luminosity samples were consistent within the error bars. The brightest galaxies (dotted line) show significant fluctuations in both real and redshift space; we think this behavior is due to the small size of the box and the low density of objects.

Figure 4 shows the dependence of $Q(\alpha)$ on galaxy luminosity in real (curves) and redshift space (points). We use the same ordinate scale for all the plots to emphasize where configuration effects are more important. The top panels show results for small scales, calculated with the L120 box. On these scales, the reduced redshift-space 3PCF of the brighter sample ($-20 > M_r^h > -21$, short dashed curve for real space, filled triangles for redshift space) is slightly lower than for the fainter sample ($-19 > M_r^h > -20$, long dashed-dotted curve for real space, filled squares for redshift space) for all angles, consistent with the results for $Q_z(r)$ using equilateral triangles. The lower plots in Figure 4 show the luminosity dependence on larger scales, measured using the L200 box; note that the luminosity bins in the lower plots are $-20 > M_r^h > -21$ and $-21 > M_r^h > -22$. The characteristic U-shape of $Q(\alpha)$ appears clearly in

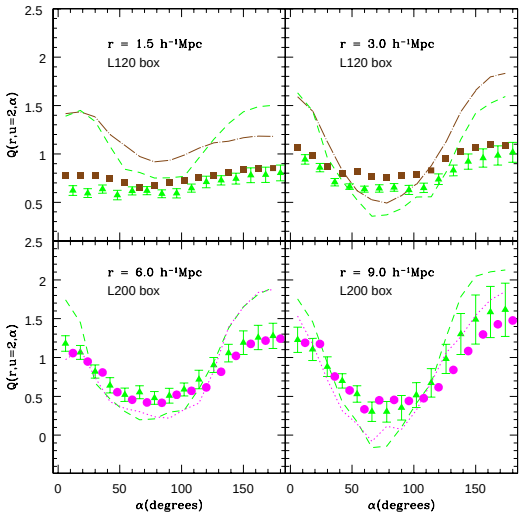


FIG. 4.— $Q(\alpha)$ shape dependence for galaxies divided by luminosity, for $r$ = 1.5, 3, 6, and 9 $h^{-1}$Mpc, with fixed $u = 2$ in real (lines) and redshift space (symbols). Top two plots are results for the L120 box: *filled squares and long dash-dotted (cyan):* $-19 > M_r^h > -20$; *filled triangles and short-dashed (green):* $-20 > M_r^h > -21$; triangles are slightly shifted to the right for clarity. Bottom plots show results for the L200 box: *filled triangles and short-dashed (green):* $-20 > M_r^h > -21$; *filled circles and dotted (magenta):* $-21 > M_r^h > -22$; circles are slightly shifted to the right for clarity. Error bars are calculated using jack-knife resampling and are shown only for one of the samples.

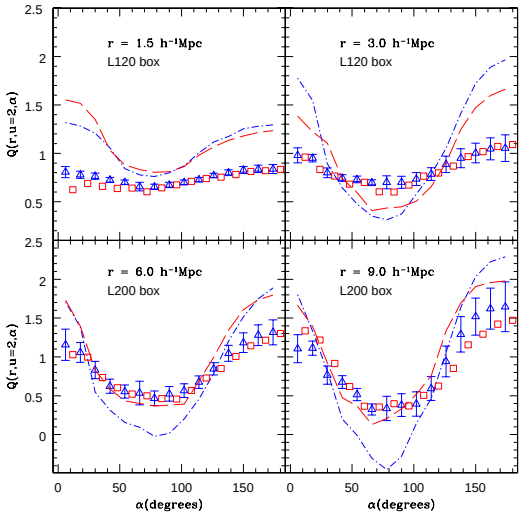


FIG. 5.— $Q(\alpha)$ shape dependence for galaxies divided by color, in the L120 box (top) and L200 box (bottom) in real (lines) and redshift space (symbols). *Open squares and long-dashed line (red):* red ($g - r > 0.7$) galaxies. *open triangles and short dash-dotted (blue):* blue ($g - r < 0.7$) galaxies; squares are slightly shifted to the right for clarity. Error bars are calculated using jack-knife resampling and are shown only for one of the samples.

the redshift-space measurements on scales larger than $r = 6$ $h^{-1}$Mpc. The luminosity dependence of $Q$ on these scales appears non-existent in redshift space and only slight in real space. There are hints that the reduced 3PCF for fainter galaxies may have slightly higher amplitude and stronger shape dependence than for brighter galaxies, but these trends are not statistically significant in the samples studied here. Rather, the strong luminosity dependence observed for the 2PCF (Zehavi et al. 2005) appears to be closely matched by a correponding dependence of the 3PCF, such that the reduced 3PCF $Q$ is roughly independent of luminosity.

### 4.2. *Color dependence*

The right panels of Figure 3 show the reduced 3PCF $Q(r)$ for equilateral triangles separately for red and blue galaxies in real (top) and redshift space (bottom). Due to limited statistics, we use the full luminosity range in each color bin, as opposed to Kayo et al. (2004), who divided the color bins into luminosity subsamples as well (see their Figure 9). Since the luminosity functions for red and blue galaxies differ, our red and blue samples have different characteristic luminosities — the red sample is on average brighter. In both real and redshift space, the red galaxies appear to have a slightly higher reduced 3PCF amplitude. Comparing with the left panels, this difference is in the opposite sense from that expected from the fact that the red galaxies are brighter; put another way, if we were to compare red and blue samples of the *same* luminosity, the color difference in $Q$ would likely be larger than that seen here. On the other hand, we should not overinterpret these trends, since the differences are within the statistical errors. Kayo et al. (2004) found a similarly weak dependence of $Q$ in redshift space on color.

Figure 5 shows the color dependence of $Q(\alpha)$ in real (curves) and redshift space (points), for the same samples and configurations as in Figure 4. In real space, on scales larger than about 3 $h^{-1}$ Mpc, $Q$ for red galaxies is larger for rectangular configurations and smaller for elongated configurations than for blue galaxies. This behavior is qualitatively consistent with a picture in which red galaxies preferentially occupy the inner regions of clusters, while blue galaxies tend to trace out more elliptical or filamentary structures. In redshift space, the trend with color is largely washed out. These redshift space results appear more consistent with the observations of the 2dFGRS (Gaztañaga et al. 2005), where the color differences for $Q$ in redshift space are smaller than those seen in the SDSS by Kayo et al. (2004).

The fact that red galaxies have a larger two-point clustering amplitude than blue galaxies and that the reduced 3PCF for red galaxies is also larger than for blue galaxies (at least for rectangular configurations) suggests that red galaxies have a larger quadratic (non-linear) bias, Cf. eqn. 10. This is qualitatively consistent with the observed morphology-density or color-density relation according to which red galaxies are preferentially found in dense regions, since the latter contribute more strongly to the higher-order correlations. The qualitative agreement between the two- and three-point observations and our method for assigning galaxy colors confirms that the color of a galaxy, a consequence of many physical processes occurring inside the galaxies, depends largely on the surrounding environment. However, we note that the color assignment for these subhalos is the most uncertain part of the model; future work will be required to determine how clustering statistics will change if more sophisticated schemes are adopted.

### 4.3. *Redshift distortions: Galaxy Type and Evolution*

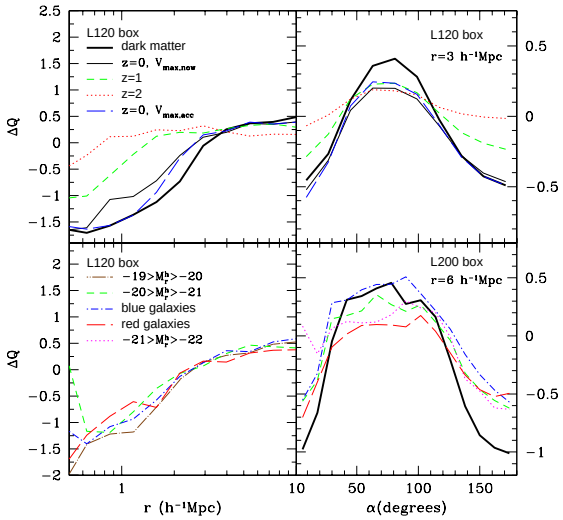


FIG. 6.— $\Delta Q(r, u, \alpha)$ as a function of galaxy type and redshift. *Top:* $\Delta Q$ for dark matter at $z = 0$ and for galaxy samples at different redshifts in the L120 box, for equilateral triangles (*top left*) and as a function of angle for triangles with $r = 3\ h^{-1}$Mpc and $u = 2$ (*top right*). *Bottom:* $\Delta Q$ as a function of galaxy type for equilateral triangles in the L120 box (*bottom left*) and as a function of angle for $r = 6\ h^{-1}$Mpc and $u = 2$ in the L200 box (*bottom right*).

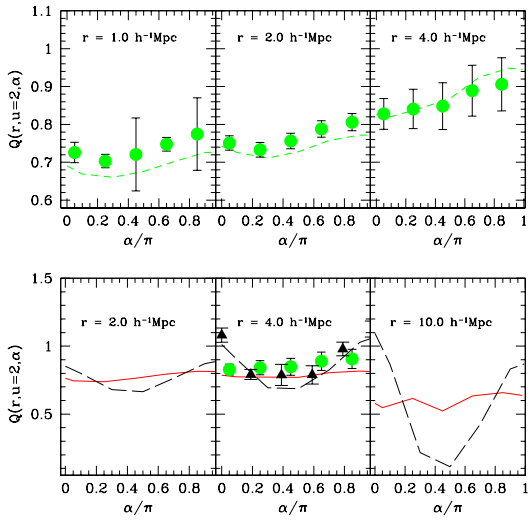


FIG. 7.— *Top:* $Q_z(r, u = 2, \alpha)$ at $r = 1.0$, 2.0 and 4.0 $h^{-1}$Mpc from SDSS observations (green points) from Nichol et al. (2006) and from our pseudo-flux-limited-sample in the L120 box (long-dashed lines) with the same binning scheme used in the mentioned paper. *Bottom:* Effect of binning in the 3PCF measurements. $Q_z(r, u = 2, \alpha)$ at $r = 2.0$ and 4.0 $h^{-1}$Mpc in the L120 box and $r = 10\ h^{-1}$Mpc in the L200 box for the simulations in a volume-limited sample. *solid (red):* results using a wide binning scheme (Nichol et al. 2006); *long-dashed (black):* results with narrow binning. In the middle panel, we plot the results using SDSS data with wide (green points) and narrow (triangles) binning.

So far, we have explored some differences between measurements in real and redshift space of the 3PCF for different simulated galaxy samples. Here we investigate in more detail whether the redshift distortions of the 3PCF are universal or instead depend on the type of galaxy studied and to what extent they evolve with time. We study the behavior of the quantity

$$\Delta Q(r, u, \alpha) \equiv Q_z(r, u, \alpha) - Q_r(r, u, \alpha), \qquad (8)$$

where $Q_r$, $Q_z$ represent the reduced 3PCF measured in real and redshift space, respectively. We explore $\Delta Q$ as a function of galaxy type (luminosity and color) and epoch. Figure 6 shows $\Delta Q$ for equilateral triangles as a function of scale and also the configuration dependence for triangles with fixed $r$, $u = 2$, and different opening angles $\alpha$.

In general, the trends are similar to those seen above: $Q_z < Q_r$ for small scales and for elongated triangle configurations, while the opposite behavior is seen for larger scales and for rectangular configurations. At $z = 0$, for equilateral triangles $\Delta Q(r)$ appears to display a roughly universal scale dependence, independent of galaxy type, with $\Delta Q(r) \simeq 0.67r^{-2} - 2.6r^{-1} - 0.02r + 0.88$ over the range $0.5 \leq r \leq 5\ h^{-1}$Mpc. On the other hand, for $r = 6h^{-1}$ Mpc and $u = 2$, the shape dependence of $\Delta Q$ shows more dependence on galaxy type, with blue galaxies having larger values than red galaxies and bright galaxies smaller values than faint galaxies. Note that the redshift distortions of $Q$ appear insensitive to whether the subhalos are identified at the present or at the time they are first accreted onto host halos.

We see clear evolution of $\Delta Q$ with redshift, as expected since redshift distortion effects should become more pronounced as perturbations become more non-linear. For equilateral triangles, the upper left panel of Figure 6 shows that the scale $r$ where $\Delta Q \sim 0$ increases with time. The shape dependence of $\Delta Q$ at fixed scale also appears to increase with time.

## 5. OBSERVING THE 3PCF: COMPARISON TO SDSS DATA AND BINNING EFFECTS

Below, we compare our results with measurements of the 3PCF from the SDSS by Nichol et al. (2006). The SDSS sample is magnitude limited, with $m_r < 17.5$, and has additional cuts in absolute magnitude, $-19 < M_r < -22$, and in redshift, $0.05 < z < 0.15$. In order to compare with this data, we randomly resample the galaxies from the L120 simulation (in particular, the $V_{max,noew}$ sample at $z = 0$), so that they have the same absolute magnitude distribution as the SDSS flux-limited sample used in Nichol et al. (2006); we call these pseudo-flux-limited samples. This resampling technique does not properly model the distance-dependent selection function of the SDSS, but it should reproduce its clustering properties on average. Moreover, since, as we have just shown, the luminosity dependence of the reduced 3PCF is weak, we expect that this procedure should be sufficiently accurate for our purposes.

Nichol et al. (2006) measure the shape dependence of $Q(\alpha)$ for four different length scales, using wide bins in $r, u$, and $\alpha$ (see their paper for more details): $\Delta r = 1$ $h^{-1}$Mpc, $\Delta u = 1$ and $\Delta\alpha = 0.1$ rad. In Figure 7, we compare the SDSS results (green points) to the calculation of $Q_z(r, u = 2, \alpha)$ using our model redshift-space, volume-limited sample 3PCF (solid lines) and our pseudo-magnitude-limited sample (dotted line), each *with the same binning as the data*. We use the L120 box for small scales and the L200 box for the $r = 10\ h^{-1}$Mpc measurements. As the top panels of Figure 7 show, the model and data show good agreement within the model jack-knife error bars in amplitude as well as in the shape of $Q(\alpha)$.

Over the range of scales shown here, both the SDSS

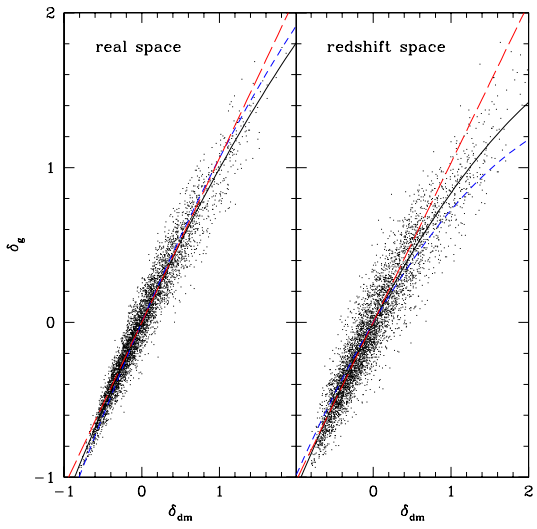


FIG. 8.— Galaxy vs. dark matter overdensities for all galaxies in the L200 box measured in randomly placed spheres of radius $10h^{-1}$ Mpc in real (left panel) and redshift space (right panel). Solid black curve denotes best fit using the quadratic bias relation of eqn. 9. Long-dashed red line indicates the best linear bias fit ($b_2 = 0$) to the 2PCF, i.e., estimating $b_1^2 = \xi_{gal}/\xi_{dm}$. Short-dashed blue curve indicates best fit of eqn. 10 to the 3PCF of the galaxies and dark matter.

data and the simulations show relatively little shape dependence for the reduced 3PCF amplitude. This is in contrast to the results of §4 above and to the 2dFGRS results of Gaztañaga et al. (2005) on similar scales, where a significantly stronger shape dependence of $Q(\alpha)$ is evident. As noted by Gaztañaga & Scoccimarro (2005) and Kulkarni et al. (2007), the differences can be traced to the binning scheme: the relatively wide binning scheme used here results in smearing and therefore suppression of the U-shape of $Q$ over most scales of interest. This effect is not due primarily to the binning in $\alpha$: small bins in both $r$ and $u$ are necessary to see the effects of shape-dependent clustering.

To illustrate these effects in more detail, in the lower panels of Figure 7 we also show results for the same sample but with a narrower binning scheme, using $\Delta r = 0.1\ h^{-1}$Mpc (ten times smaller), $\Delta u = 0.2$ (five times smaller), and $\Delta\alpha = 0.05$ rad (two times smaller). With the narrower bins (shown by the dashed curves in Figure 7), the shape-dependence of $Q$ is more pronounced for the simulation, especially on larger scales. For comparison, for $r = 4\ h^{-1}$Mpc (lower center panel), the solid triangles shows results for the SDSS flux-limited sample using a similar narrow binning scheme Nichol et al. (2006), again showing good agreement between the model and the data.

## 6. GALAXY BIAS AND THE 3PCF

As we have seen, the 3PCF predicted for galaxies differs systematically from that expected for dark matter. These differences reflect differences in the spatial distributions of these two populations; higher-order statistics can therefore provide important constraints upon the bias between galaxies and dark matter (Fry & Gaztanaga 1993; Frieman & Gaztanaga 1994) and its dependence upon galaxy properties.

On large scales, where the rms dark matter and galaxy overdensities are small compared to unity, it is common to adopt a deterministic, local bias model (e.g. Fry & Gaztanaga 1993),

$$\delta_{gal} = f(\delta_{dm}) = b_1\delta_{dm} + \frac{b_2}{2}\delta_{dm}^2 + ..., \qquad (9)$$

where $\delta_{gal}$ and $\delta_{dm}$ are the local galaxy and dark matter overdensities smoothed over some scale $R$. We can use the simulations above to test how well this simple bias prescription characterizes the galaxy distribution and its clustering statistics.

Figure 8 shows the relation between $\delta_{gal}$ and $\delta_{dm}$ for all subhalos in the L200 box. The points show the overdensities for the galaxy and dark matter fields in randomly placed spheres of radius $10h^{-1}$ Mpc in both real (left panel) and redshift space (right panel). The solid black curves show the best quadratic fits of the form in eqn. (9). The quadratic local bias model appears to do a reasonable job in characterizing the mean relation. Nonetheless, there is significant scatter, either due to stochastic bias or dependence of bias on other properties than $\delta_{dm}$, that is not captured by this simple bias model. The errors on these fits, also extended to samples divided by galaxy luminosity, are shown in Fig. 9 by the light solid contours.

To leading order, this bias prescription leads to a relation between the galaxy and dark matter reduced 3PCF amplitudes of the form (Fry & Gaztanaga 1993; Gaztañaga & Scoccimarro 2005)

$$Q_{gal} = \frac{1}{c_1}\left(Q_{dm} + c_2\right), \qquad (10)$$

where $c_1 = b_1$ and $c_2 = b_2/b_1$. Also to leading order, at low overdensities the relation between the galaxy and dark matter 2PCF amplitudes in this model is given just by the linear bias, $\xi_{gal} = b_1^2\xi_{dm}$. We can test how well this bias prescription captures the clustering statistics by fitting these relations to the dark matter and galaxy 2- and 3-point correlation functions in the simulation in both real and redshift space and extracting the parameters $c_1$ and $c_2$. Since the relation (9) holds for the density fields on some smoothing scale, we should fit the correlation functions for separations comparable to or slightly larger than this scale. For the 3PCF, we use triangles with $u \equiv r_{23}/r_{12} = 2$, $r = 9\ h^{-1}$Mpc, and weight equally all configurations with $0^0 < \alpha < 180^0$ using the L200 box. To calculate the likelihood function, we use a method similar to that described in Gaztañaga & Scoccimarro (2005), which is based on an eigenmode analysis of the covariance matrix. We use the jack-knife subsamples in real and redshift space to construct covariance matrices, and we use only the dominant eigemodes with values $> \sqrt{2/N}$ where $N = 16$ is the number of jack-knife subsamples; we found that adding further eigenmodes just increases artificially the signal.

The best-fit parameter values from the 3PCF, substituted into Eqn. 9, are shown as the short-dashed blue curves in Figure 8. Also, in the right panels of Figure 2 we show the predicted galaxy 3PCF (solid blue curves) using the measured dark matter $Q_{dm}$ and the best fitting $c_1, c_2$ parameters in Eqn. (10) from the fit at $r = 9h^{-1}$ Mpc. We see that the agreement with the measured galaxy 3PCF is very good in both real and redshift space for triangles with $r = 9h^{-1}$ Mpc; for configurations

TABLE 2
Best-fit bias parameters in the L200 box

| Subample | $c_1^Q$ | $c_2^Q$ | $c_1^\delta$ | $c_2^\delta$ | $c_1^\xi$ |
|---|---|---|---|---|---|
| All objects r-space | 1.16 | -0.19 | 1.10 | -0.20 | 1.06 |
| All objects z-space | 0.86 | -0.31 | 0.97 | -0.32 | 1.03 |
| $-20 < M_r^h < -21$ r-space | 1.08 | -0.20 | 1.04 | -0.08 | 1.01 |
| $-20 < M_r^h < -21$ z-space | 0.86 | -0.30 | 1.01 | -0.34 | 1.00 |
| $-21 < M_r^h < -22$ r-space | 1.42 | -0.15 | 1.21 | -0.36 | 1.19 |
| $-21 < M_r^h < -22$ z-space | 0.99 | -0.20 | 1.01 | -0.43 | 1.13 |

with $r = 6h^{-1}$ Mpc, the agreement in real space is still quite good while in redshift space some deviations in the shape-dependence appear.

In Figure 9 we show the fits for $c_1$ and $c_2$ for the different galaxy samples in the L200 box in both real and redshift space: all galaxies (top panels), galaxies in the absolute range $-20 > M_r^h > -21$ (middle), and those in the range $-21 > M_r^h > -22$ (bottom). The thick oval contours indicate the 1 and $2\sigma$ confidence intervals for a $\Delta\chi^2$ distribution with two free parameters, constrained using the 3PCF, via Eq. (10), and the large points indicate the maxiumum likelihood values from the 3PCF. The thin solid contours show the constraints on $c_1$ and $c_2$ using the fit of Eq. (9) to the measurements in Figure 8, and the vertical line in each panel shows the estimate of $c_1$ from comparing the 2PCF amplitudes for galaxies and dark matter using pairs selected from the triplets used to measure the 3PCF. The best-fit values are shown in Table 2: the first two columns show the best-fit parameters $c_1^Q$, $c_2^Q$ using the reduced 3PCF (eq. 10), the next two columns, $c_1^\delta$ and $c_2^\delta$, are calculated using the quadratic bias model (eq. 9) fit to the counts in cells, and in the last column $c_1^\xi$ is obtained from comparing the 2PCF of galaxies and dark matter assuming a linear bias model, $c_1^2 = \xi_{gal}/\xi_{dm}$.

In agreement with previous measurements in surveys and simulations, the bias parameters obtained from the 3PCF are degenerate, resulting in elongated contour ellipses; this could be mitigated to some extent by using a larger variety of triangle configurations. In real space (left panels of Figure 9), we see that the three methods of extracting the bias parameters are in rough agreement: there is a preference for $c_1 \sim 1$ and negative $c_2$ as was found for the 2dFGRS 3PCF measurements (Gaztañaga et al. 2005). Note that the 3PCF fit tends to overestimate $c_1$ and to slightly overestimate $c_2$ compared to the other two methods. In redshift space (right panels), the opposite is true: the 3PCF constraint tends to underestimate $c_1$. The right panels of Figs. 8 and 9 show that there is a larger discrepancy between the 3PCF fits and the counts-in-cells fit to Eqn. (9) in redshift space, suggesting that the relation (10) may not be a good representation in redshift space.

While this comparison with the deterministic local bias model is suggestive, to test it more quantitatively one should use more triangle configurations and larger-volume catalogs to enable more precise calculation of the correlation matrices.

## 7. SUMMARY

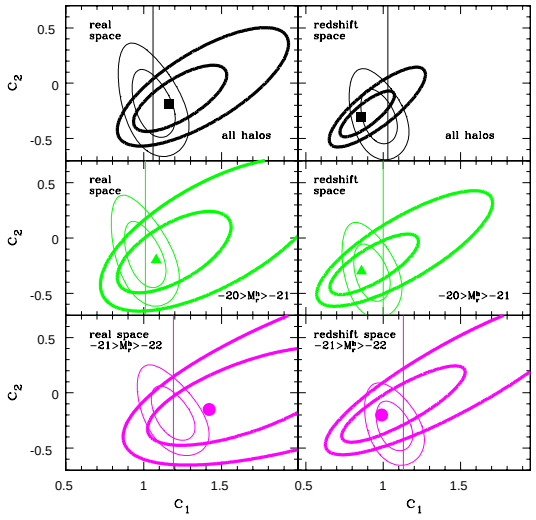


Fig. 9.— Constraints on the model bias parameters $c_1$ and $c_2$ in real (left panels) and redshift space (right panels), measured in the L200 box for all galaxies (top), galaxies with $-20 > M_r^h > -21$ (middle), and galaxies with $-21 > M_r^h > -22$ (bottom). Thick ellipses correspond to $1\sigma$ and $2\sigma$ constraints on parameters using the reduced 3PCF fit to equation 10; symbols denote the minimum $\chi^2$ value. Thin ellipses come from fitting the smoothed halo and dark matter overdensities (equation 9) shown in Figure 8. The vertical lines show the constraint on $c_1$ from comparing the dark matter and galaxy 2PCF amplitudes and fitting the ratio with a linear bias model, $c_1^2 = \xi_{gal}/\xi_{dm}$.

We have studied the 3PCF of dark matter and galaxies in high-resolution dissipationless cosmological simulations. The galaxy model associates dark matter halos with galaxies by matching the halo velocity function, including subhalos, with the observed galaxy luminosity function by abundance, and has been shown previously to provide an excellent match to observed two-point statistics for galaxies (Conroy et al. 2006). Our primary results are as follows:

1. The reduced real-space 3PCF for both galaxies and dark matter has strong dependence on scale and shape. The shape dependence of the 3PCF strengthens with increasing scale, in agreement with previous simulation results for dark matter and with expectations from non-linear perturbation theory.

2. On small scales, or alternatively with increasing time, the shape dependence of $Q$ washes out as virial motions within halos replace coherent infall on larger scales.

3. Redshift-space distortions attenuate the shape and scale dependence of the reduced 3PCF and weaken the evolution with redshift.

4. The reduced 3PCF shows only weak dependence on galaxy luminosity and color; put another way, the scaling between the 3PCF amplitude and the 2PCF is predicted to be nearly independent of galaxy type in this model. The trend of $Q$ with color is somewhat stronger than with luminosity: the reduced 3PCF is slightly enhanced for red galaxies over blue, especially for elongated configurations.

5. Our model predictions are in excellent agreement with the shape and scale dependence of the galaxy 3PCF measured in the SDSS when the same binning scheme is used. Since the results are highly sensitive to the binning scheme, caution must be exercised in comparing theory and observations of the 3PCF. In combination with earlier results, this comparison indicates that a simple scheme in which galaxies and dark matter halos and subhalos are associated in a one-to-one fashion based on maximum circular velocity can provide a good match to a wide range of galaxy clustering statistics.

6. The effect on the 3PCF of changing the selection of subhalos (*i.e.,* of connecting galaxy luminosity to $V_{max,acc}$ instead of $V_{max,now}$) is evident on small scales ($r < 2\ h^{-1}$Mpc) and for elongated configurations, but is negligible on larger scales. Future measurements of the 3PCF will help constrain different models for the association of galaxy luminosity and color with subhalo properties.

7. On scales of order $10h^{-1}$ Mpc, a local, deterministic bias scheme is in reasonable agreement with the galaxy and dark matter distributions of the model. The bias parameters extracted from $Q_{gal}$ are in reasonable agreement with the $\delta_{gal}$-$\delta_{dm}$ relation in real space, less so in redshift space. Nevertheless, the redshift-space constraints on the bias parameters are in agreement with the 2dFGRS measurements of the 3PCF.

We are indebted to Anatoly Klypin and Brandon Allgood for running and making available the simulations used in this paper, which were run on the Columbia machine at NASA Ames and on the Seaborg machine at NERSC (Project PI: Joel Primack), to Andrey Kravtsov for running some of the halo catalogs used in this study, and to Charlie Conroy for providing us with measurements of $v_{\rm max,acc}$. We thank Enrique Gaztañaga for enlightening comments on measuring and interpreting the 3PCF and comparing results of $Q(\alpha)$ with his estimator; and Cameron McBride for discussions on the measurements of the bias parameters. We additionally thank Andrey Kravtsov, Issha Kayo and Roman Scoccimarro for several useful discussions. RHW was partially supported by NASA through Hubble Fellowship grant HST-HF-01168.01-A awarded by the Space Telescope Science Institute, and also recieved support from the U.S. Department of Energy under contract number DE-AC02-76SF00515. This work was supported in part by the Kavli Institute for Cosmological Physics through the grant NSF PHY-0114422. FAM thanks the Fulbright Program and CONICYT-Chile for additional support.

This study also made use of the SDSS DR3 Archive, for which funding has been provided by the Alfred P. Sloan Foundation, the Participating Institutions, the National Aeronautics and Space Administration, the National Science Foundation, the U.S. Department of Energy, the Japanese Monbukagakusho, and the Max Planck Society. The SDSS Web site is http://www.sdss.org/. The SDSS is managed by the Astrophysical Research Consortium (ARC) for the Participating Institutions: the University of Chicago, Fermilab, the Institute for Advanced Study, the Japan Participation Group, the Johns Hopkins University, Los Alamos National Laboratory, the Max-Planck-Institute for Astronomy (MPIA), the Max-Planck-Institute for Astrophysics (MPA), New Mexico State University, University of Pittsburgh, Princeton University, the United States Naval Observatory, and the University of Washington. We also made extensive use of the NASA Astrophysics Data System and of the `astro-ph` preprint archive at `arXiv.org`.

REFERENCES

Abazajian, K., et al. 2003, AJ, 126, 2081
Allgood, B., Flores, R. A., Primack, J. R., Kravtsov, A. V., Wechsler, R. H., Faltenbacher, A., & Bullock, J. S. 2006, MNRAS, 367, 1781
Barriga, J., & Gaztañaga, E. 2002, MNRAS, 333, 443
Baugh, C. M., et al. 2004, MNRAS, 351, L44
Berlind, A. A., & Weinberg, D. H. 2002, ApJ, 575, 587
Bernardeau, F., Colombi, S., Gaztañaga, E., & Scoccimarro, R. 2002, Phys. Rep., 367, 1
Berrier, J. C., Bullock, J. S., Barton, E. J., Guenther, H. D., Zentner, A. R., & Wechsler, R. H. 2006, ApJ, 652, 56
Blanton, M. R. et al. 2003a, AJ, 125, 2348
Blanton, M. R., et al. 2003b, ApJ, 592, 819
Colless, M., et al. 2001, MNRAS, 328, 1039
Conroy, C., Wechsler, R. H., & Kravtsov, A. V. 2006, ApJ, 647, 201
—. 2007, ApJ, submitted, arXiv:astro-ph/0703374
Croton, D. J., Norberg, P., Gaztanaga, E., & Baugh, C. M. 2006, ArXiv Astrophysics e-prints
Croton, D. J., et al. 2004, MNRAS, 352, 1232
da Ângela, J., Outram, P. J., Shanks, T., Boyle, B. J., Croom, S. M., Loaring, N. S., Miller, L., & Smith, R. J. 2005, MNRAS, 360, 1040
Feldman, H. A., Frieman, J. A., Fry, J. N., & Scoccimarro, R. 2001, Physical Review Letters, 86, 1434
Frieman, J. A., & Gaztañaga, E. 1999, ApJ, 521, L83
Frieman, J. A., & Gaztanaga, E. 1994, ApJ, 425, 392
Fry, J. N., & Gaztanaga, E. 1993, ApJ, 413, 447
Gaztañaga, E., Norberg, P., Baugh, C. M., & Croton, D. J. 2005, MNRAS, 364, 620
Gaztañaga, E., & Scoccimarro, R. 2005, MNRAS, 361, 824
Gaztanaga, E., & Frieman, J. A. 1994, ApJ, 437, L13
Gray, A. G., Moore, A. W., Nichol, R. C., Connolly, A. J., Genovese, C., & Wasserman, L. 2004, in ASP Conf. Ser. 314: Astronomical Data Analysis Software and Systems (ADASS) XIII, 249
Hikage, C., Matsubara, T., Suto, Y., Park, C., Szalay, A. S., & Brinkmann, J. 2005, PASJ, 57, 709
Hou, Y. H., Jing, Y. P., Zhao, D. H., & Börner, G. 2005, ApJ, 619, 667
Huterer, D., Knox, L., & Nichol, R. C. 2001, ApJ, 555, 547
Jing, Y. P., & Borner, G. 1997, A&A, 318, 667
Jing, Y. P., & Börner, G. 1998, ApJ, 503, 37
—. 2004, ApJ, 607, 140
Kayo, I. et al. 2004, PASJ, 56, 415
Klypin, A., Gottlöber, S., Kravtsov, A. V., & Khokhlov, A. M. 1999, ApJ, 516, 530
Kravtsov, A. V., Berlind, A. A., Wechsler, R. H., Klypin, A. A., Gottlöber, S., Allgood, B., & Primack, J. R. 2004, ApJ, 609, 35
Kravtsov, A. V., Klypin, A. A., & Khokhlov, A. M. 1997, ApJS, 111, 73
Kulkarni, G. V., Nichol, R. C., Sheth, R. K., Seo, H.-J., Eisenstein, D. J., & Gray, A. 2007, ApJ, submitted; arXiv:astro-ph/0703340
Landy, S. D., & Szalay, A. S. 1993, ApJ, 412, 64
Matsubara, T., & Suto, Y. 1994, ApJ, 420, 497
Moore, A. W. et al. 2001, in Mining the Sky, 71
Nichol, R. C. et al. 2006, MNRAS, 368, 1507
Nishimichi, T., Kayo, I., Hikage, C., Yahata, K., Taruya, A., Jing, Y. P., Sheth, R. K., & Suto, Y. 2006, ArXiv Astrophysics e-prints
Pan, J., & Szapudi, I. 2005, MNRAS, 362, 1363

Peebles, P. J. E. 1980, The Large-Scale Structure of the Universe (Princeton University Press)
Peebles, P. J. E., & Groth, E. J. 1975, ApJ, 196, 1
Ross, A. J., Brunner, R. J., & Myers, A. D. 2006, ApJ, 649, 48
Scoccimarro, R., Colombi, S., Fry, J. N., Frieman, J. A., Hivon, E., & Melott, A. 1998, ApJ, 496, 586
Scoccimarro, R., Couchman, H. M. P., & Frieman, J. A. 1999, ApJ, 517, 531
Scoccimarro, R., Feldman, H. A., Fry, J. N., & Frieman, J. A. 2001, ApJ, 546, 652
Sefusatti, E., Crocce, M., Pueblas, S., & Scoccimarro, R. 2006, Phys. Rev. D, 74, 023522
Sefusatti, E., & Scoccimarro, R. 2005, Phys. Rev. D, 71, 063001
Suto, Y., & Matsubara, T. 1994, ApJ, 420, 504
Szapudi, I. 2005, arXiv:astro-ph/0505391
Szapudi, I., Postman, M., Lauer, T. R., & Oegerle, W. 2001, ApJ, 548, 114
Szapudi, I., et al. 2002, ApJ, 570, 75
Szapudi, S., & Szalay, A. S. 1998, ApJ, 494, L41
Takada, M., & Jain, B. 2003, MNRAS, 340, 580
Tasitsiomi, A., Kravtsov, A. V., Wechsler, R. H., & Primack, J. R. 2004, ApJ, 614, 533
Tinker, J. L. 2007, MNRAS, 374, 477
Vale, A., & Ostriker, J. P. 2004, MNRAS, 353, 189
—. 2006, MNRAS, 371, 1173
Verde, L., Heavens, A. F., Matarrese, S., & Moscardini, L. 1998, MNRAS, 300, 747
Verde, L. et al. 2002, MNRAS, 335, 432
Wang, Y., Yang, X., Mo, H. J., van den Bosch, F. C., & Chu, Y. 2004, MNRAS, 353, 287
Wechsler, R. H. 2004, in Clusters of Galaxies: Probes of Cosmological Structure and Galaxy Evolution, ed. J. S. Mulchaey, A. Dressler, & A. Oemler
Wechsler, R. H., Zentner, A. R., Bullock, J. S., Kravtsov, A. V., & Allgood, B. 2006, ApJ, 652, 71
York, D. G., et al. 2000, AJ, 120, 1579
Zehavi, I., et al. 2005, ApJ, 630, 1
Zheng, Z. 2004, ApJ, 610, 61